Atomic-scale study of electric dipoles near charged and uncharged domain walls in ferroelectric films

CHUN-LIN JIA[1]*, SHAO-BO MI[1], KNUT URBAN[1], IONELA VREJOIU[2], MARIN ALEXE[2] AND DIETRICH HESSE[2]

[1]Institute of Solid State Research and Ernst Ruska Centre for Microscopy and Spectroscopy with Electrons, Research Centre Jülich, D-52425 Jülich, Germany

[2]Max Planck Institute of Microstructure Physics, Weinberg 2, D-06120 Halle, Germany

*e-mail: c.jia@fz-juelich.de

Published online: 9 December 2007; doi:10.1038/nmat2080

Ferroelectrics are materials exhibiting spontaneous electric polarization due to dipoles formed by displacements of charged ions inside the crystal unit cell. Their exceptional properties are exploited in a variety of microelectronic applications. As ferroelectricity is strongly influenced by surfaces, interfaces and domain boundaries, there is great interest in exploring how the local atomic structure affects the electric properties. Here, using the negative spherical-aberration imaging technique in an aberration-corrected transmission electron microscope, we investigate the cation–oxygen dipoles near 180° domain walls in epitaxial $PbZr_{0.2}Ti_{0.8}O_3$ thin films on the atomic scale. The width and dipole distortion across a transversal wall and a longitudinal wall are measured, and on this basis the local polarization is calculated. For the first time, a large difference in atomic details between charged and uncharged domain walls is reported.

Ferroelectric thin films find potential applications in electronic and electro-optical devices including, for example, non-volatile and high-density memories, thin-film capacitors and piezoelectric and pyroelectric devices[1–3]. The performance of such devices depends strongly on the magnitude and stability of the switchable ferroelectric polarization of the ferroelectric layer. Polarization switching is realized by nucleation and growth of polarization domains under an external electrical field[4–6]. To this end, the properties of the domain walls, in particular their structure, width and mobility, are important parameters. In bulk ferroelectrics, the paraelectric to ferroelectric phase transition is accompanied by the formation of polarization domains to minimize the system energy with respect to the depolarization field and mechanical strain. Because of the six equivalent cubic ⟨100⟩ directions that can be chosen as directions for the polarization dipoles in $PbTiO_3$ and $Pb(Zr_xTi_{1-x})O_3$, both 90° and 180° domain walls occur, where, on passing the wall from one domain to the other, the polarization vector changes direction by about 90° and 180°, respectively. In thin films, the formation of domains depends strongly on processing conditions and constraints arising from the substrate/film orientation relationship and crystal lattice misfit. A 90° domain structure was observed in $PbTiO_3$ and $Pb(Zr_xTi_{1-x})O_3$ films on various substrates[7–9]. Stripes of 180° domains of alternating polarity were reported for thin films of $PbTiO_3$ on $SrTiO_3$ (refs 10,11).

The structure of 90° domain walls was studied by lattice-fringe imaging in the electron microscope[7,12] in $PbTiO_3$ and $BaTiO_3$ (ref. 13). In this work, the atomic structure of the walls could not be resolved owing to a lack of instrumental resolution. Nevertheless, the tetragonal distortion of the lattice was measured across the walls, from which their width could be deduced. The 180° domain walls are particularly important for the understanding of polarization switching under an external electrical field[4–6]. In fact, 180° domains and domain boundaries in ferroelectric materials (for example, $BaTiO_3$, $PbTiO_3$, $LiTaO_3$, $LiNbO_3$), and corresponding inverse domains and domain boundaries in non-ferroelectric polar dielectrics (for example, ZnO, GaN) were investigated in the electron microscope. Early work made use of Bragg diffraction contrast either under such dark-field conditions where Friedel's law is not valid[14–17] or by observation of contrast fringes at the domain boundaries[18,19]. More recent work used lattice-fringe imaging[20,21]. However, owing to instrument-based limitations, these investigations had to be carried out at a resolution far from an atomic level. On the other hand, the width of 180° domain walls in trigonal $LiTaO_3$ ferroelectrics was investigated using scanning nonlinear dielectric microscopy and was reported to be 1–2 nm (ref. 22).

Recently, it has been shown[23,24] that atomic resolution including oxygen can be achieved by a novel technique called negative spherical-aberration (C_S) imaging in a C_S-corrected transmission electron microscope[25]. For this purpose, a small negative value of the spherical aberration of the objective lens is adjusted. Combining this with an objective-lens overfocus yields negative phase-contrast images showing the atomic columns seen end-on and bright on a dark background[26]. Using this technique, we investigate the atomic details and dipole distortion on an atomic scale near 180° domain walls in thin epitactic films of $PbZr_{0.2}Ti_{0.8}O_3$ sandwiched between two $SrTiO_3$ layers and prepared by pulsed laser deposition[27] (see the Methods section and Supplementary Information).

Figure 1a shows the approximately 10-nm-thick $PbZr_{0.2}Ti_{0.8}O_3$ layer between the two $SrTiO_3$ layers. The viewing direction is along the crystallographic $[\bar{1}10]$ direction. The interfaces are marked by two horizontal arrows. The two insets show magnifications overlying the respective areas in the upper left, domain I, and

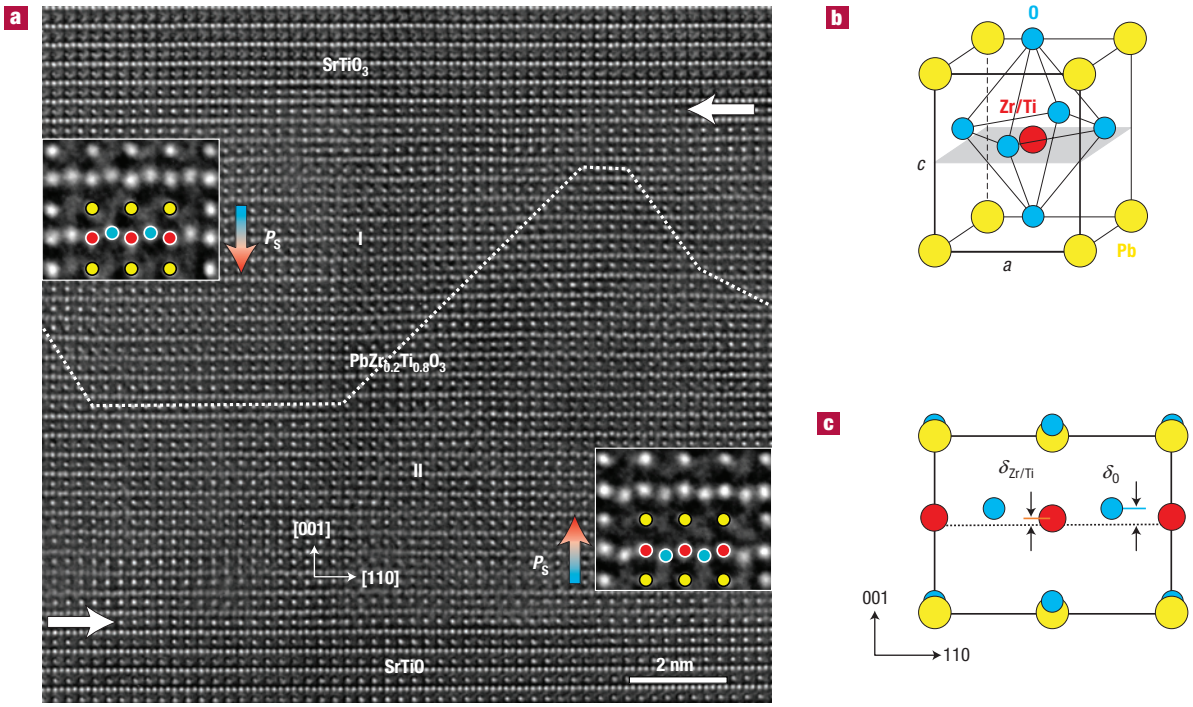

Figure 1 Atomic-scale imaging of the electric dipoles formed by the relative displacements of the Zr/Ti cation columns and the O anion columns. a, Image of a $SrTiO_3/PbZr_{0.2}Ti_{0.8}O_3/SrTiO_3$ thin-film heterostructure. The image is recorded under negative spherical-aberration imaging conditions with the incident electron beam parallel to the $[\bar{1}10]$ direction. The atom columns appear bright on a dark background. The horizontal arrows denote the horizontal interfaces between the $PbZr_{0.2}Ti_{0.8}O_3$ and the top and the bottom $SrTiO_3$ film layers. The dotted line traces the 180° domain wall. The arrows denoted by 'P_S' show the directions of the polarization in the 180° domains. The insets show magnifications of the dipoles formed by the displacements of ions in the unit cells (yellow: PbO, red: Zr/Ti, blue: O). **b**, Schematic perspective view of the unit cell of ferroelectric $PbZr_{0.2}Ti_{0.8}O_3$. **c**, Projection of the unit cell along the $[\bar{1}10]$ direction. $\delta_{Zr/Ti}$ and δ_O denote the shifts of the Zr/Ti atoms and the oxygen atoms, respectively, from the centrosymmetric positions.

the lower right side of the figure, domain II. Yellow symbols denote PbO atom columns seen end-on. Red symbols denote Zr/Ti columns and blue symbols represent oxygen. As illustrated by the schematic diagrams in Fig. 1b,c, the atom arrangement exhibits shifts of the atoms with respect to the cubic perovskite structure. In domain I (left inset), the Zr/Ti atom columns are shifted upward (along the [001] direction) towards the upper PbO positions and away from the respective lower ones. The oxygen atoms are also shifted upward but more strongly and thus are no longer collinear with the Zr/Ti atoms. This results in a reduction of the symmetry of the atom arrangement from cubic to tetragonal with the four-fold axis parallel to [001]. We note that in the epitactic thin-film system of $PbZr_{0.2}Ti_{0.8}O_3$ on $SrTiO_3$ this is only an approximation. Owing to biaxial coherency strain, the symmetry of $PbZr_{0.2}Ti_{0.8}O_3$ changes during the transition from the paraelectric to the ferroelectric state from centrosymmetric tetragonal to non-centrosymmetric tetragonal. The new atom arrangement leads to a separation of the centre of the anionic negative charge of oxygen from that of the cationic positive charge of the metal cations. The corresponding charge dipoles define the direction of the vector of spontaneous polarization $\mathbf{P}_S$ (pointing from net negative to net positive charge) parallel to [001]. The atom shifts in domain II (right inset) are in the opposite direction compared with those in domain I. In fact, the area of the $PbZr_{0.2}Ti_{0.8}O_3$ film layer in Fig. 1a contains two polarization domains where, on changing from one domain to the other, the polarization vector changes by 180°. The position of the respective 180° domain wall, indicated by a dotted line, can be determined directly by mapping the atomic displacements. In our study, which also included films of 5 nm and 20 nm thickness, we exclusively observed the 180° inversion polarization domain structure, and no 90° domain orientations were found.

With respect to the habit plane, three types of 180° domain-wall morphology are observed. In the first (horizontal segments in Fig. 1a), in the following termed 'longitudinal domain wall' (LDW), the normal of the domain-wall plane is parallel to the polarization vector in the two domains. Across this type of wall, the electric dipoles are head-to-head or tail-to-tail, resulting in a nominally charged domain wall. (Usually it is assumed that internal mobile charges, for example, oxygen vacancies or electronic carriers, compensate for the polarization charges at head–head- or tail–tail-coupled boundaries. Domain walls of this type have been suggested to be stabilized by three- or five-valent elements[28].) In the second type, termed 'transversal domain wall' (TDW), the normal is perpendicular to the polarization vectors, so that the domain wall is head–tail coupled and not charged. Most frequently observed are planar and curved domain walls of 'mixed character' where the habit plane normal makes an arbitrary angle with the polarization vectors. A closer inspection shows that this type of domain wall consists of LDW and TDW segments.

Figure 2a shows a mixed character domain wall (dotted line) consisting of TDW segments, whose habit plane is parallel to the (110) plane. Their vertical extension is c, $2c$ and $3c$, where c denotes the c-axis lattice parameter. These are separated by short (001) LDW segments of horizontal width $a\sqrt{2}/2$, where a denotes the a-axis lattice parameter. The TDW segments run parallel to the $[\bar{1}10]$ viewing direction and are seen edge-on. As indicated

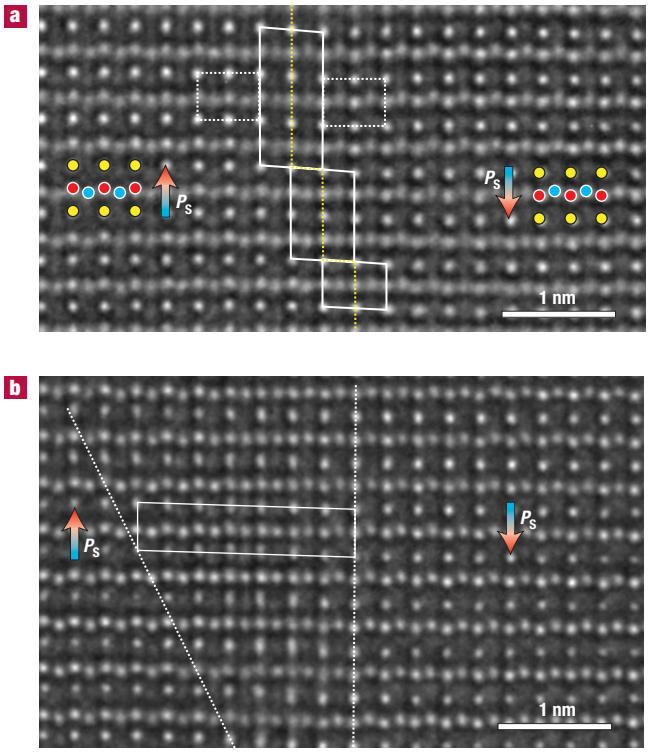

Figure 2 [$\bar{1}$10] images of domain-wall segments of mixed type. a, A narrow domain wall seen edge-on. The arrows 'P_S' indicate the opposite polarization directions across the domain wall. The parallelograms denote the segments of TDW. The yellow dotted line marks the central plane of the domain wall. The white dotted lines trace projected unit cells on either side of the domain wall. These are undistorted indicating that the domain-wall width is just one projected unit cell. **b**, Image of an inclined domain wall of mixed character. The dotted lines mark the lines along which the wall cuts through the upper and the lower surface of the specimen. The parallelogram tracing the Pb atoms indicates the atom shifts in the wall area. The image of the projected Pb-atom columns is strongly elongated owing to the overlap of two adjoining domains along the viewing direction.

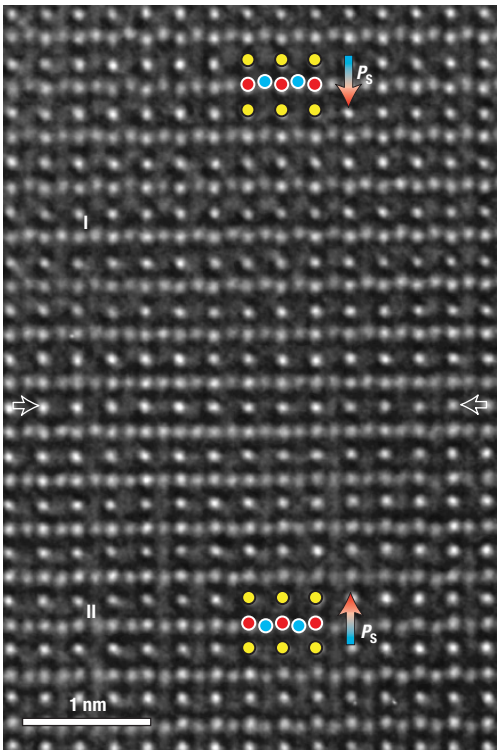

Figure 3 Image of an LDW segment. Arrows denote the geometric central plane of the wall, which is referred to as the origin for quantitative analysis of the dipole distortion across the wall area.

by the vertical shift of the oxygen atoms, 'down' on the left and 'up' on the right-hand side, the width of the wall is just one projected unit cell ($a\sqrt{2}$). This is corroborated by quantitative measurements of the vertical displacements $\delta_{Zr/Ti}$ of the Zr/Ti and δ_O of the O atoms (defined in Fig. 1c). Although no displacement can be measured in the wall centre (dotted yellow line in Fig. 2a), the values approach the 'normal' ones (far from the wall) of $\delta_{Zr/Ti} \approx 0.01$ nm and $\delta_O \approx 0.038$ nm within the next projected unit cell (dotted white line) on either side of the wall. Viewing the figure at a glancing angle from left to right, it can be recognized that on passing the domain wall, the Zr/Ti atom rows parallel to [110] show only a slight shift, whereas the Pb atom rows are strongly shifted in the direction of the polarization vector. This is also indicated by the parallelogram-type distortion of the cells indicating the wall segments. Figure 2b shows a more complicated case. Inspection of the atomic shifts indicates that at the left side of the figure, the polarization vector is pointing upward, whereas it is pointing downward on the other side. Between the dotted lines, the Pb atoms are shifted in a similar way as just described for the TDW. This is indicated by the parallelogram tracing out the Pb positions. We also find that across the width of the wall area, the image of the Pb-atom rows is smeared out along the vertical [001] direction. This can be understood assuming that the habit plane of this domain wall of mixed character is inclined and therefore the two domains overlap along the viewing direction.

Figure 3 shows an LDW (a section of the wall on the left side of Fig. 1a). The arrows indicate the geometrical centre of the wall. From the fact that the atomic maxima are sharp and undistorted, we infer that this wall is imaged edge-on. We take the following steps for quantitative measurements of the lattice parameters and the atomic shifts as a function of vertical distance from the wall centre. First, we carry out a least-squares fit by two-dimensional gaussian profiles to each of the individual atomic intensity profiles in the figure[29]. The position of all the maxima of the gaussians defines the experimental data set of atomic positions in the image. On this basis, all of the parameters defined in Fig. 1b,c, that is, the *c*- and *a*-axis lattice parameter as well as the two shift parameters $\delta_{Zr/Ti}$ of the Zr/Ti and δ_O of the O atoms, can be determined for each of the unit cells shown in Fig. 3. As we are only interested in the behaviour of these parameters as a function of distance from the domain-wall centre, we calculate for a certain distance from the central plane a mean value by taking the average of the contrast-maximum position data parallel to the domain wall over the horizontal width of Fig. 3.

However, for ultrahigh precision measurements, we have to take into account that owing to residual objective-lens aberrations and an unavoidable small deviation of the crystallographic zone axis from the direction of the incident electron beam, the positions of the contrast maxima in the image may deviate slightly from the real atomic positions. To eliminate these artefacts, a model structure of the domain wall is constructed and the image expected from

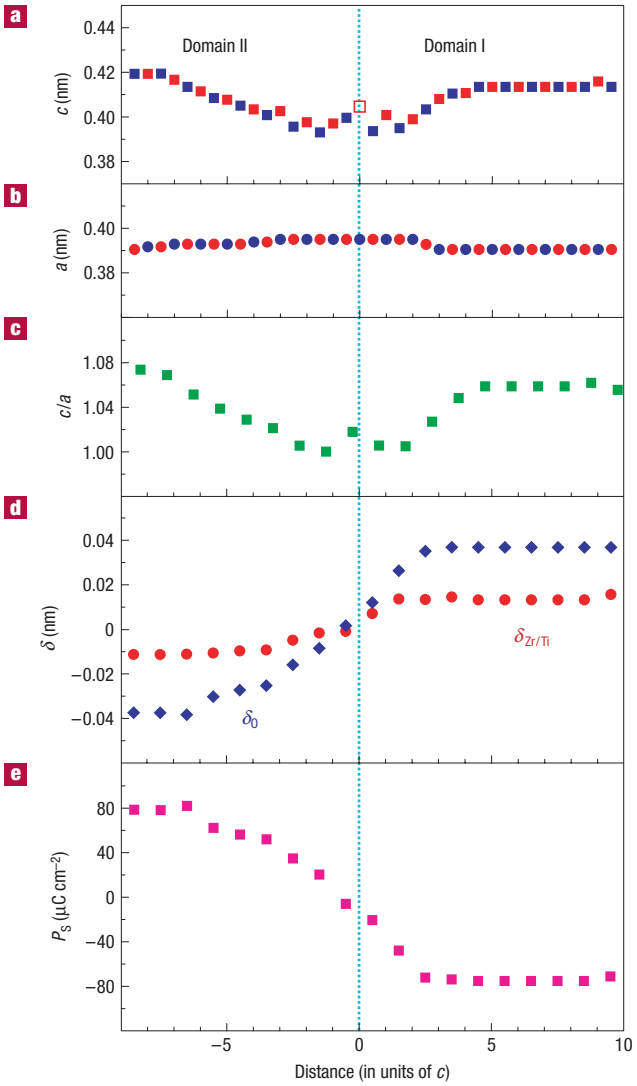

Figure 4 Quantities of the structural and electric behaviour of the LDW as a function of the distance expressed in units of *c* from the central plane of the LDW shown in Fig. 3. a, *c*-axis lattice parameter. Blue squares and red squares show the values measured from Pb to Pb atom positions and from Zr/Ti to Zr/Ti, respectively. **b**, *a*-axis lattice parameter. Blue circles and red circles show the values measured from Pb to Pb atom positions and from Zr/Ti to Zr/Ti, respectively. Gaussian regression analysis indicates a measurement error of better than 5 pm (see ref. 21 and Supplementary Information). **c**, Tetragonality c/a calculated from **a** and **b**. **d**, The displacements of the Zr/Ti atoms ($\delta_{Zr/Ti}$) and the O atoms (δ_0) across the LDW. Positive values denote upward shifts and negative values downward shifts. **e**, The spontaneous polarization P_S calculated on the basis of the *c*-lattice parameters and the atomic displacements shown in **a** and **d**. The positive values represent upward polarization and the negative values downward polarization.

this structure is calculated using quantum-mechanical and optical image simulations in which the imaging parameters are treated as variables. An iterative procedure is carried out in which the model and the imaging parameters are adjusted until a best fit between calculated and experimental data is reached[30]. A detailed discussion of this procedure including measurement errors is provided in the Supplementary Information. In the following, we present the data of the structure determined in this way. The accuracy of such an ultrahigh-resolution quantitative image analysis has been investigated by a careful gaussian regression analysis and is found to be better than 5 pm for a 95% confidence level of the values derived[29].

In Fig. 4a, blue squares denote measurements of the *c*-axis lattice parameter carried out on PbO atomic positions. Red squares denote measurements on Zr/Ti positions. The distances are calibrated with reference to the lattice parameter (0.3905 nm) of the $SrTiO_3$ layers.

The minimum value of *c* occurs in the domain-wall centre with an accompanying increase of the *a*-axis lattice parameter, as shown in Fig. 4b. The increase of *a* can also be seen by viewing Fig. 3 at a glancing angle from bottom to top. With increasing distance from the central area, *c* increases adopting a plateau value of about 0.413 nm in domain I. In domain II this value is 1.3% higher. This results in a maximum tetragonality value of $c/a = 1.059$ in domain I and 1.072 in domain II (Fig. 4c). We note that the value for the Zr/Ti separation in the wall centre adopts a local maximum (open square in Fig. 4a). This is a geometrical effect because the two inner Zr/Ti atom rows belonging to different domains are shifted in opposite directions. In addition, in the central area of four to five unit cells in width, the *c* spacings between the Zr/Ti atom columns are larger than those between the PbO columns. This is due to the continuous increase of the Zi/Ti shift away from the centre. In this area, the average value of *c* is about 0.397 nm and that of *a* is about 0.395 nm, leading to a value of 1.005 for c/a. Figure 4d shows the values of the vertical displacements $\delta_{Zr/Ti}$ and δ_O as a function of the vertical separation from the domain-wall plane. These displacements show essentially the same behaviour as *c*, that is, they follow the tetragonality, with the exception of the central area of four to five unit cells where the increase of the displacements is not accompanied by an increase of the *c* value. Considering the variation of *c*, we infer a width of the LDW of 3*c* (domain I) plus 7*c* (domain II), considerably wider than the respective value for the TDW.

Figure 4e shows the spontaneous polarization versus distance from the central plane of the domain wall. The values of $\mathbf{P}_S$ are calculated on the basis of the *c*-axis lattice parameters and the atomic displacements shown in Fig. 4a,d and the effective charge values of the ions for $PbTiO_3$ given in ref. 31. The maximum value of the modulus of $\mathbf{P}_S$ is about 75 μC cm^{-2} for domain I and about 80 μC cm^{-2} for domain II. Inside the domain wall, the polarization changes direction. Interestingly, in the central area four to five unit cells wide, the polarization grows from zero to about 40 μC cm^{-2}, whereas the tetragonality ($c/a = 1.005$) remains essentially constant.

According to our results, the width of the TDW is found to be of the order of one unit cell. This is in excellent agreement with first-principles total-energy calculations[32,33] and with a calculation based on the scaling law for ferroic stripe domains[34] for the TDW, indicating an abrupt change of polarization direction across the wall. With respect to the habit plane, the lowest energy was found for {100} planes and a slightly higher energy for {110} planes. The sharp atomic image of Fig. 2a clearly indicates a (110) habit plane. The elongated contrast of the PbO atomic columns in Fig. 2b is likewise compatible with {110}-type facets. However, {100} habit planes cannot be ruled out. The facets in the mixed character domain wall in Fig. 2a correspond to the previously unobserved steps anticipated in early theories[35,36] for the motion of 180° walls in ferroelectric switching in $BaTiO_3$.

Previous experimental studies on the 180° domains were focused on the TDW as it is generally assumed that the formation of the LDW is hampered by the fact that any tilt of the wall habit plane away from that of the ideal TDW induces local charge due to the head-to-head or tail-to-tail configuration of the polarization across the wall. In the extreme case of the LDW,

the energy due to the uncompensated charge in the wall should be too high to allow its formation. However, it was recently shown by first-principles density-functional calculations, that, in $PbTiO_3$, the head-to-head or tail-to-tail LDW could be stabilized by substitution of Ti^{4+} by, respectively, three- or five-valent elements drawn from neighbouring columns in the periodic table[28]. For example, for the acceptor Sc^{3+}, stable head-to-head domain walls of widths as low as two unit cells were calculated. We note that irrespective of their lengths, all of the LDW segments observed in our $Pb(Zr_xTi_{1-x})O_3$ films are of the head-to-head type. The fact that these walls have a width of the order of 10 unit cells can be understood in terms of their particular charge status. First, the system energy can be reduced by distributing the polarization charge over an extended thickness of the wall. This is supported by the strong reduction of the *c*-axis lattice parameter and therefore the tetragonality in the wall area. We note that titanium can reduce its valency from normally Ti^{4+} to Ti^{3+}, allowing it to contribute to charge compensation in a manner similar to scandium.

The possible mechanism for LWD formation can be derived from the particular sample geometry taking into account the kinetics of domain formation. In the $PbZr_{0.2}Ti_{0.8}O_3$ layer constrained between the two $SrTiO_3$ layers, nucleation of ferroelectric domains occurs at both interfaces. During subsequent growth, domains nucleated at different interfaces meet forming segments of TWD and LWD, where the latter is stabilized by local three-valent titanium cations. We note that lattice defects can also influence the structure and width of a domain wall[37]. However, in our investigations, no extended defects are observed at the wall areas, nor do we find any indication of aggregation of point defects or local deviation of the occupancy of Ti/Zr sites from the statistical average.

Finally, we want to point out that the possibility of imaging the local polarization dipoles at atomic resolution, quantitatively measuring the local polarization and thus investigating the domain structure provides a quantitative basis for studying the mechanism of polarization switching and other properties such as coercive field and ferroelectric fatigue.

METHODS

The triple-layer films of $SrTiO_3/PbZr_{0.2}T_{0.8}O_3/SrTiO_3$ were grown on (001) $SrTiO_3$ substrates by pulsed laser deposition. Under the deposition conditions, a remnant polarization as high as 105 $\mu C\,cm^{-2}$ was measured by dynamic polarization hysteresis measurements, carried out under electric field, on epitaxial $PbZr_{0.2}T_{0.8}O_3$ films thicker than 20 nm that had been grown on $SrRuO_3$-coated $SrTiO_3$ (001) single crystals. Details of the growth are given elsewhere[27]. The ⟨110⟩ cross-sectional specimens for high-resolution transmission electron microscopy investigation were prepared by standard procedures including mechanical grinding, dimpling and polishing. The final thinning of the specimens by Ar-ion milling was carried out on a stage cooled with liquid nitrogen. High-resolution transmission electron microscopy investigation was carried out on an FEI Titan 80-300 microscope with a C_S corrector for the objective lens. The available point resolution is better than 0.08 nm at an operating voltage of 300 kV. Images were recorded by a 2k × 2k CCD (charge-coupled device) camera with a sampling rate of 0.01 nm per pixel. All of the images presented here are Fourier-filtered to minimize the effect of the contrast noise. The filtering does not have any effect on the results of our measurements (see the Supplementary Information). Structure modelling and image simulations were carried out using the CrystalKit-MacTempas software package[38].

Received 8 August 2007; accepted 6 November 2007; published 9 December 2007.

References

1. Setter, N. & Waser, R. Electroceramic materials. *Acta Mater.* **48**, 151–178 (2000).
2. Dawber, M., Rabe, K. M. & Scott, J. F. Physics of thin-film ferroelectric oxides. *Rev. Mod. Phys.* **77**, 1083–1130 (2005).
3. Scott, J. F. Applications of modern ferroelectrics. *Science* **315**, 954–959 (2007).
4. Roelofs, A. *et al.* Depolarizing-field-mediated 180 degrees switching in ferroelectric thin films with 90 degrees domains. *Appl. Phys. Lett.* **80**, 1424 (2001).
5. Jung, D. J., Dawber, M., Scott, J. F., Sinnamon, L. J. & Gregg, J. M. Switching dynamics in ferroelectric thin films: An experimental survey. *Integrat. Ferroelectr.* **48**, 59–68 (2002).
6. Gysel, R., Stolichnov, I., Setter, N. & Pavius, M. Ferroelectric film switching via oblique domain growth observed by cross-sectional nanoscale imaging. *Appl. Phys. Lett.* **89**, 082906 (2006).
7. Stemmer, S., Streiffer, S. K., Ernst, F. & Rühle, M. Atomistic structure of 90° domain walls in ferroelectric $PbTiO_3$ thin films. *Phil. Mag. A* **71**, 713–724 (1995).
8. Foster, C. M. *et al.* Single-crystal $Pb(Zr_xTi_{1-x})O_3$ thin films prepared by metalorganic chemical vapor deposition: Systematic compositional variation of electronic and optical properties. *J. Appl. Phys.* **81**, 2349–2357 (1997).
9. Lee, K. S., Choi, J. H., Lee, J. Y. & Baik, S. Domain formation in epitaxial $Pb(Zr, Ti)O_3$ thin films. *J. Appl. Phys.* **90**, 4095–4102 (2001).
10. Streiffer, S. K. *et al.* Observation of nanoscale 180° stripe domains in ferroelectric $PbTiO_3$ thin films. *Phys. Rev. Lett.* **89**, 67601–67604 (2002).
11. Fong, D. D. *et al.* Ferroelectricity in ultrathin perovskite films. *Science* **304**, 1650–1653 (2004).
12. Foeth, M., Sfera, A., Stadelmann, P. & Buffat, P.-A. A comparison of HREM and weak beam transmission electron microscopy for the quantitative measurement of the thickness of ferroelectric domain walls. *J. Electron Microsc.* **48**, 717–723 (1999).
13. Floquet, N. *et al.* Ferroelectric domain walls in $BaTiO_3$: Fingerprints in XRPD diagrams and quantitative HRTEM image analysis. *J. Physique III* **7**, 1105–1128 (1997).
14. Tanaka, M. & Honjo, G. Electron optical studies of barium titanate single crystal films. *J. Phys. Soc. Japan* **19**, 954–970 (1964).
15. Tanaka, M. Contrast of 180° domains of $PbTiO_3$ in an electron microscopic image. *Acta Cryst. A* **31**, 59–63 (1975).
16. Gevers, R., Blank, H. & Amelinckx, S. Extension of the Howie–Whelan equations for electron diffraction to non-centro symmetrical crystals. *Phys. Status Solidi* **13**, 449–465 (1966).
17. Serneels, R. *et al.* Friedel's law in electron diffraction as applied to the study of domain structures in non-centrosymmetrical crystals. *Phys. Status Solidi B* **58**, 277–292 (1973).
18. Wicks, B. J. & Lewis, M. H. Direct observations of ferroelectric domains in lithium niobate. *Phys. Status Solidi* **26**, 571–576 (1968).
19. Bursill, L. A. & Lin, P. J. Electron microscopic studies of ferroelectric crystals. *Ferroelectric* **70**, 191–203 (1986).
20. Sanchez, A. M., Ruterana, P., Benamara, M. & Strunk, H. P. Inversion domains and pinholes in GaN grown over Si(111). *Appl. Phys. Lett.* **82**, 4471–4473 (2003).
21. Liu, Y. Z. *et al.* Inversion domain boundary in a ZnO film. *Phil. Mag. Lett.* **87**, 687–693 (2007).
22. Daimon, Y. & Cho, Y. Cross-sectional observation of nanodomain dots formed in both congruent and stoichiometric $LiTaO_3$ crystals. *Appl. Phys. Lett.* **90**, 192906 (2007).
23. Jia, C. L., Lentzen, M. & Urban, K. Atomic-resolution imaging of oxygen in perovskite ceramics. *Science* **299**, 870–873 (2003).
24. Jia, C. L. & Urban, K. Atomic-resolution measurement of oxygen concentration in oxide materials. *Science* **303**, 2001–2004 (2004).
25. Haider, M. *et al.* Electron microscopy image enhanced. *Nature* **392**, 768–769 (1998).
26. Jia, C. L., Lentzen, M. & Urban, K. High-resolution transmission electron microscopy using negative spherical aberration. *Microsc. Microanal.* **10**, 174–184 (2004).
27. Vrejoiu, I. *et al.* Intrinsic ferroelectric properties of strained tetragonal $PbZr_{0.2}Ti_{0.8}O_3$ obtained on layer-by-layer grown, defect-free single-crystalline films. *Adv. Mater.* **18**, 1657–1661 (2006).
28. Wu, X. & Vanderbilt, D. Theory of hypothetical ferroelectric superlattices incorporating head-to-head and tail-to-tail 180° domain walls. *Phys. Rev. B* **73**, 020103 (2006).
29. Houben, L., Thust, A. & Urban, K. Atomic-precision determination of the reconstruction of a 90° tilt boundary in $YBa_2Cu_3O_{7-\delta}$ by aberration corrected HRTEM. *Ultramicroscopy* **106**, 200–214 (2006).
30. Williams, D. B. & Carter, C. B. *Transmission Electron Microscopy* (Plenum, New York and London, 1996).
31. Zhong, W., King-Smith, R. D. & Vanderbilt, D. Giant LO-TO splittings in perovskite ferroelectrics. *Phys. Rev. Lett.* **72**, 3618–3621 (1994).
32. Pöykkö, S. & Chadi, D. J. Ab initio study of 180° domain wall energy and structure in $PbTiO_3$. *Appl. Phys. Lett.* **75**, 2830–2832 (1999).
33. Meyer, B. & Vanderbilt, D. Ab initio study of ferroelectric domain walls in $PbTiO_3$. *Phys. Rev. B* **65**, 104111 (2002).
34. Catalan, G., Scott, J. F., Schilling, A. & Gregg, J. M. Wall thickness dependence of the scaling law for ferroic stripe domains. *J. Phys. Condens. Matter* **19**, 02201 (2007).
35. Miller, R. C. & Weinreich, G. Mechanism for the sidewise motion of 180-degrees domain walls in barium titanate. *Phys. Rev.* **117**, 1460–1466 (1960).
36. Hayashi, M. Kinetics of domain wall motion in ferroelectric switching. 1. General formulation. *J. Phys. Soc. Japan* **33**, 616 (1972).
37. Gopalan, V., Dierolf, V. & Scrymgeour, D. A. Defect-domain wall interactions in trigonal ferroelectrics. *Annu. Rev. Mater. Res.* **37**, 449–89 (2007).
38. O'Keefe, M. A. & Kilaas, R. Advances in high-resolution image simulation. *Scan Microsc. Suppl.* **2**, 225–244 (1988).

Acknowledgements

The authors thank L. Houben for continuous support in using the software package for image mapping. Correspondence and requests for materials should be addressed to C.-L.J.
Supplementary Information accompanies this paper on www.nature.com/naturematerials.